atmosphere

Article

Mesoscale Observational Analysis of Isolated Convection Associated with the Interaction of the Sea Breeze Front and the Gust Front in the Context of the Urban Heat Humid Island Effect

Nan Zhang [1], Yan Wang [2,3,*] and Xiaomeng Lin [1]

[1] Tianjin Meteorological Observatory, Tianjin 300074, China; nanzhangnanzhang@163.com (N.Z.); littlelemon0526@163.com (X.L.)
[2] Tianjin Weather Modification Office, Tianjin 300074, China
[3] Tianjin Key Laboratory for Oceanic Meteorology, Tianjin 300074, China
* Correspondence: swallownx@163.com

Abstract: An isolated convection was unexpectedly initiated in the evening of 1 August 2019 around the Tianjin urban region (TUR), which happened at some distance from the shear line at lower level and the preexisting convection to the South, analyzed by using ERA5 reanalysis data and observations from surface weather stations, and a S-band radar. The results show that, 42 min before the initiation of the convection, the atmospheric thermodynamic conditions around TUR were favorable for the initiation of the isolated convection, although the southerly and vertical shear of the horizontal wind at the lower level was weak. A sea-breeze front approached the TUR and continued to move West, leading to the triggering of the isolated convection in the context of the urban humid heat island (UHHI) effect. Subsequently, the gust front, which was formed between the cold pool away from the TUR and the warm and humid air of the UHHI, moved northward, approached the convection, and collided with sea breeze front, resulting in five reflectivity centers of isolated convection being merged and the convection's development. Finally, the isolated convection split into two convections that moved away from the TUR and disappeared at 20:36 Beijing Time. The isolated convection was initiated and developed by the interaction of the sea breeze front and gust front in the context of the UHHI effect. The sea breeze front triggered the isolated convection around TUR in the context of the UHHI effect, and the gust front produced by the early convective storms to the south played a vital role in the development of the isolated convection.

Keywords: isolated convection; Tianjin urban region; sea breeze front; gust front; cold pool

Citation: Zhang, N.; Wang, Y.; Lin, X. Mesoscale Observational Analysis of Isolated Convection Associated with the Interaction of the Sea Breeze Front and the Gust Front in the Context of the Urban Heat Humid Island Effect. *Atmosphere* **2022**, *13*, 603. https://doi.org/10.3390/atmos13040603

Academic Editors: Liang Gao, Pingping Luo, Yingzhao Ma, Mengye Chen and Ji Chen

Received: 28 January 2022
Accepted: 7 April 2022
Published: 9 April 2022

1. Introduction

Rainstorms in North China, especially in the West Bank of the Bohai Sea, are characterized by their short duration, rapid generation and high intensity and being strongly localized. Most of local rainstorms are caused by small-scale or meso-scale weather systems, which are very difficult to predict. The research has showed that the convergence caused by the local terrain provides better dynamic conditions for the initiation of local storms [1,2]. The interaction between the mesoscale cold pool and easterly winds [3,4], and the triggering effect of small-scale cyclones [3] on local heavy rainfall clouds has also been studied. In addition, scholars have also studied the role of the gust front [3], dew point front [5] and sea breeze front [6] in the triggering and development of local convections. Undoubtedly, these studies have significantly advanced the understanding of rainfall-generated mesoscale convective storms. Despite the many advances in the understanding of the structure and life cycle of convections, the accurate forecasting of convective initiation remains one of the greatest challenges in meteorology [7–11], which is especially true for the convective initiation (CI) of isolated convections [12]. From 2018 to 2021, the initiation and development of isolated convection occurred many times around the Tianjin urban region (TUR) on the West Bank of the Bohai Sea, such as the convections in the afternoon of 22 July 2018, the afternoon of 18 July 2019, the evening of 1 August 2019 and the evening of 7 July 2021. The multi-scale mechanism of isolated convection around the TUR in the afternoon of 18 July 2019 was analyzed [13], and the results showed that the initiation of the isolated convection was closely related to the urban heat island (UHI) phenomenon. The resulting UHI and urban canopy effects may lead to changes in the local and regional atmospheric circulation and precipitation [14–20]. The analysis of 113 locally developed non-typhoon cyclone extreme rainfall events in the summer of 2011–2018 also shows the contribution of the UHI effect to the occurrence of more hourly extreme rainfall [21].

As everyone knows, the UHI effect is the thermal mechanism of isolated convection around urban regions; however, the exact initial time and location of isolated convective systems remain difficult to predict [12]. Previous studies have shown that the convective cloud is mainly initiated from the convergence zone in the boundary layer, such as the zone near the front and the dry line [5,6,22–31]. In addition, the sea breeze front is also one of the significant mesoscale weather systems triggering convective storms in Tianjin, as a coastal megacity in North China, and it usually causes localized storms as it moves further inland [32,33]. A lot of researches have been performed on convections caused by sea breeze fronts [6,34–39]. A three-dimensional, cloud-resolving model was used to investigate the interaction between the sea-breeze circulation and boundary layer roll convection [40,41], and the results provide further evidence that horizontal convective rolls can play an important role in the initiation and modulation of convection along a sea-breeze front. Large-eddy simulations were performed to investigate the process of deep-convection initiation over a peninsula, and the result showed that convection is produced through the collision of the sea-breeze fronts or the collision between the gust front and sea breeze front [42]. In addition, the results of a lot of researches show that sea breeze front can not only interact with dynamic systems, such as sea breeze front [42], gust front [6,35] and horizontal convective roll [40,41], but also interact with thermal systems, such as the UHI effect [13,43–47].

Nevertheless, few studies have been performed to reveal the interaction of the sea breeze front and gust front in the context of the urban humid heat island (UHHI) effect, which led to the generation and development of the isolated convection around the TUR. Thus, the present study focuses on the isolated convection around the TUR on 1 August 2019. This paper aims to better understand the role of the sea breeze front, gust front and the UHHI effect in the initiation and development of isolated convection. Moreover, this research also aims to acquire a better understanding about the physical mechanisms of this type of weather case, thus improving the ability of forecasting and early warning.

2. Dataset and Methodology

2.1. Dataset

The fifth generation of the European Center for Medium-Range Weather Forecasts (ECMWF) reanalysis database (ERA5) was used, which provides atmospheric variables at 1 h intervals. The spatial resolution of this dataset is 0.25° × 0.25°. This dataset has 37 levels in vertical direction [48]. The ERA5 data are available at https://cds.climate.copernicus.eu/#!/search?text=ERA5&type=dataset (accessed on 8 April 2020).

A total of 289 surface weather stations were used in this study, including 11 national and 278 regional observation stations, whose distribution is shown in Figure 1. These surface stations are relatively evenly distributed with an average distance of about 5 km. The meteorological elements observed by surface stations include precipitation, wind, temperature and dew point temperature at 1 h intervals. The data were interpolated into 0.1° × 0.1° grids by the inverse distance weight method in order to plot the contour map and the color map.

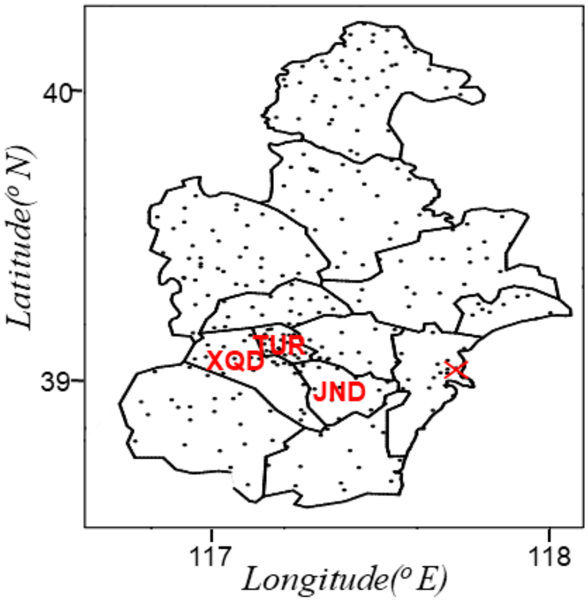

Figure 1. Distribution of weather observations (dots) used for this research and the position of the Doppler Radar in the Tanggu District (red cross). The district names of Tianjin are abbreviated on the map as follows: TUR (Tianjin urban region), XQD (Xiqing District) and JND (Jinnan District).

Additionally, the Tanggu Doppler S-band Radar was also used in this paper. The location of this radar (117.72° E, 39.04° N) is shown in Figure 1.

2.2. *Definition of Urban Humid Heat Island*

As it is well known, the "urban heat island" effect refers to the "high temperature" of the city caused by a large number of artificial heating, high heat storage bodies, such as buildings and roads, and the reduction in green spaces. The temperature in the urban region is significantly higher than that in the rural region. However, another phenomenon was identified in our research, which is also worthy of our attention, that is, that the city is located in a high temperature zone and high humidity zone (high dew point temperature or high specific humidity zone), and is neither located in the center of high temperature nor in the center of high humidity, but is located in the center of high pseudo-equivalent potential temperature, indicating that the urban region has the characteristics of high temperature and high humidity compared with the surrounding rural area. In this paper, this phenomenon was defined as the phenomenon of urban humid heat island (UHHI).

2.3. *Selection of Standard Time*

The time of Eastern Eighth Time Zone was defined Beijing Time (BT). BT is 8 h earlier than universal time, that is, BT equals universal time plus 8 h. In this paper, Beijing time was taken as the standard time to describe the convective events.

2.4. *Methodology of Creating Sounding*

Due to their higher horizontal and temporal resolutions, reanalysis soundings have been used for climatological storm environment studies by a growing number of studies [49–54]. Therefore, the present study created proximity soundings for this case, which included creating reanalysis soundings using the ERA5 reanalysis dataset and correcting the surface reanalysis soundings using 1 h surface observations. The construction of the sounding was as follows. First, 27 isobaric layers from 1000 hPa to 100 hPa of pressure, altitude, temperature, dew-point temperature, and horizontal wind at the certain grid (39° N, 117° E) and time (14:00 BT and 17:00 BT) were extracted from the ERA5 data. Next, the observation data of the surface station in the TUR were used to take the place of the lowest level data of ERA5 sounding.

3. Precipitation Observation and Associated Characteristics

Figure 2 displays the distribution of the accumulated rainfall amounts during this weather event, which was from 17:00 to 20:00 BT on 1 August 2019. The short-time strong rainfall event of interest occurred around the TUR on 1 August 2019. The 3 h (17:00 BT–20:00 BT) accumulated rainfall exhibited an isolated precipitation (the maximum rainfall intensity of 36.1 mm·h^{-1} located in Tiaoyuanli in the TUR during 18:00–19:00 BT) area, characterized by rapid generation, short duration, high strength and strong locality. Rainfall amounts in 9 stations exceeded 25 mm, while the maximum rainfall amounts of 43.8 mm appeared in the Erweilu weather station of the TUR. This type of local rainstorm in Tianjin in summer is not rare (there were four isolated convection events around the TUR from 2018 to 2021, and another three occurred at noon on 22 July 2018, in the afternoon on 18 July 2019, and in the evening on 7 July 2021), which also brings challenges to early and accurate warning.

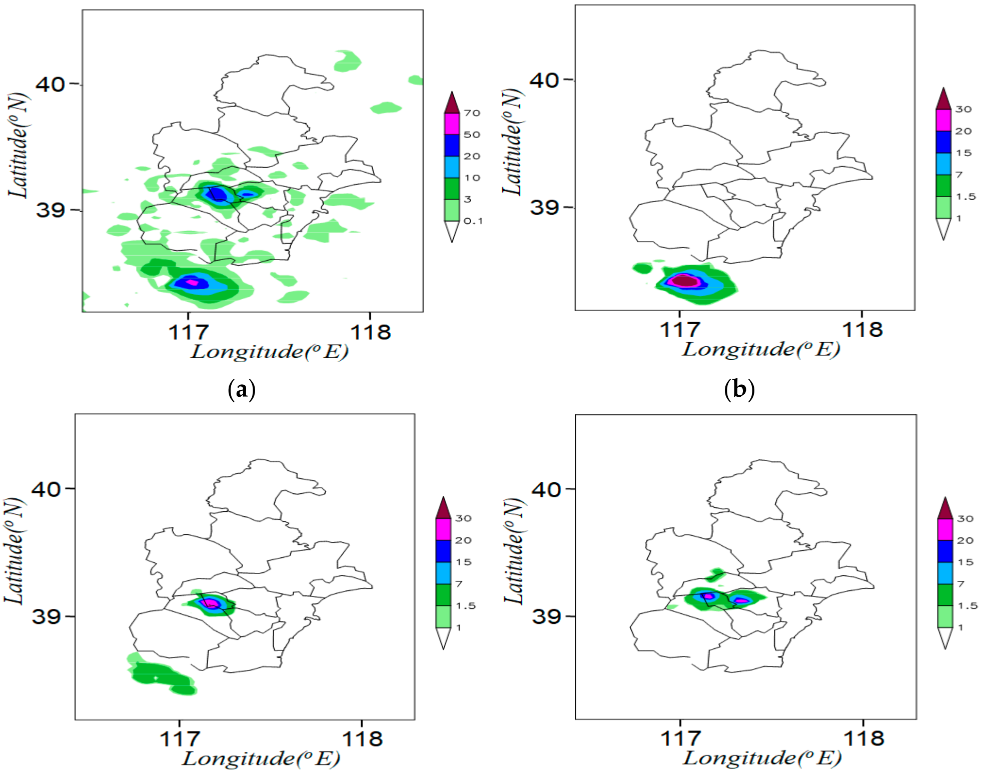

(**a**) (**b**)

(**c**) (**d**)

Figure 2. Distribution of accumulated precipitation (colored, unit: mm) (**a**) from 17:00 to 20:00 BT, (**b**) from 17:00 to 18:00 BT, (**c**) from 18:00 to 19:00 BT, (**d**) from 19:00 to 20:00 BT on 1 August 2019.

Figure 3 displays the evolution of the rainy storm observed by the Tanggu S-band Doppler Radar. As shown in Figure 3, the accumulated precipitation around the TUR was contributed by the locally developed, isolated convection during 17:40–20:00 BT on 1 August. At 17:30 BT on 1 August (see Figure 3a), a mature convective storm moving from East to West was located to the south of Tianjin, with a gust front in front of its movement and there was no convection around the TUR. The isolated convection was initiated at the junction of the TUR, XQD and JND at 17:42 BT (see Figure 3b), and the center of reflectivity was greater than 35 dBZ, reaching levels above 40 dBZ at 17:48, and located in the XQD (see Figure 3c). The continuous convection was triggered and the subsequent growth of the convections led to the convection having five centers of reflectivity, which were located in the south of the TUR, but the highest reflectivity of the convections was still 40 dBZ at 18:00 BT (see Figure 3d). From 18:06 BT (see Figure 3e) to 18:12 BT (see Figure 3f), the merging of the five reflectivity centers in the South of the TUR made the isolated convection grow into its mature stage, whose highest reflectivity reached levels of more than 55 dBz, locating at the junction of the TUR and XQD. The isolated convection moved northward from 18:12 to 18:30 BT, and the main body of the isolated convection influenced the TUR at 18:30 BT (see Figure 3g). After 19:00 BT (see Figure 3h), the isolated convection around the TUR rapidly weakened, dissipated, moved northward, and was gradually split into two convections, one (convection A) in the North of the TUR and the other (convection B) in the southeast of the TUR. After 20:00 BT (see Figure 3i), convection A moved northward, and convection B moved northeast by East. Then, the two convections gradually weakened and disappeared at 20:36 BT.

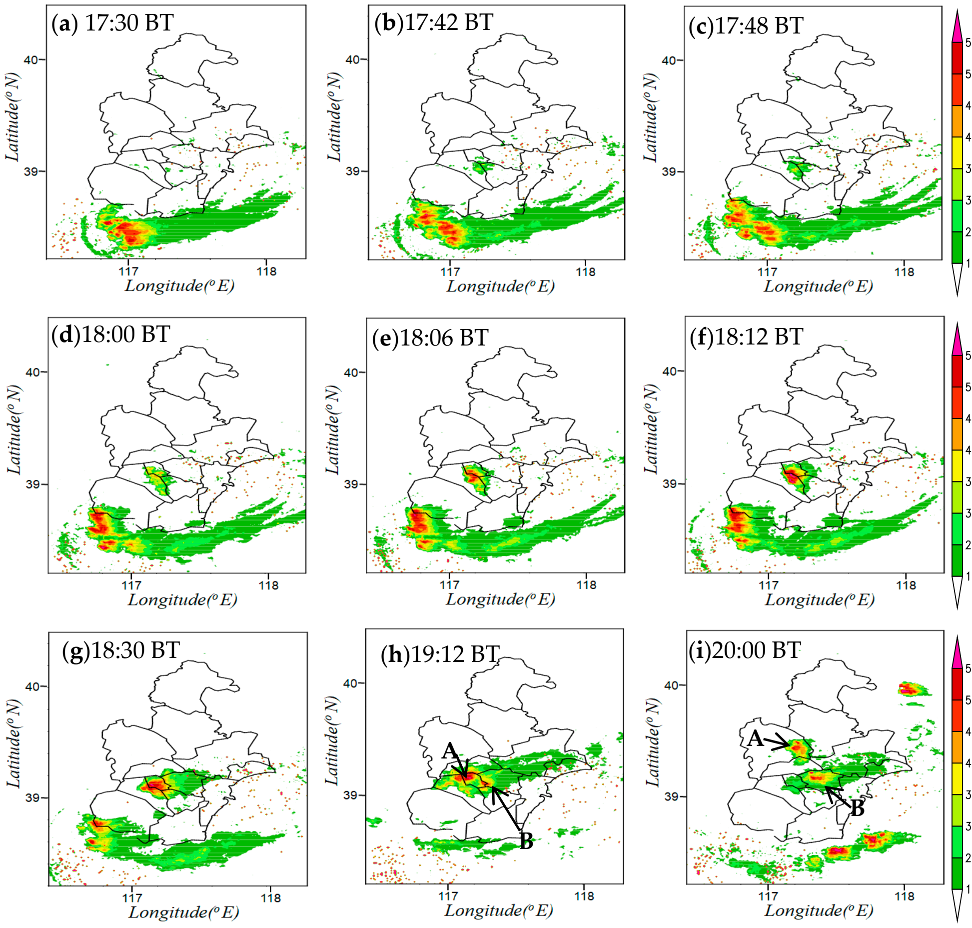

Figure 3. Composite reflectivity (colored, unit: dBZ) from the S-band Radar of Tanggu in Tianjin: (**a**) 17:30; (**b**) 17:42; (**c**) 17:48; (**d**) 18:00; (**e**) 18:06; (**f**) 18:12; (**g**) 18:30; (**h**) 19:12; (**i**) 20:00 BT. "A" and "B" represent the position of two convections.

4. Synoptic Background

The major features of the synoptic conditions in the lower and middle troposphere (from 1000 hPa to 500 hPa) before the isolated convection was formed are displayed in Figure 4. The yellow pentagram in Figure 4 is used to indicate the position of the TUR. At 14:00 BT on 1 August, the TUR was located in the area of high pseudo-equivalent potential temperature with a weak southerly flow and about 250 km away from a 925 hPa convergence line to the north. The convergence line (red dashed line in Figure 4a,b) remained at about 43° N~44° N (see Figure 4a). Due to the imbalance of wind fields on the north and south sides of the western part of the convergence line at this time, 3 h later (42 min before the initiation of the convection, 17:00 BT), the western part of the convergence line was obviously moving southward (from 43° N to 41° N), but the eastern part was moving very slowly, so the distance between the convergence line and the TUR had no significant change, which suggests that the boundary of the low-level convergence line or baroclinic zone never intruded the TUR, while the isolated convection was initiated. In addition, as shown in Figure 4c,d, 3 h before the initiation of the isolated convection, the atmosphere of the middle level and low level were always in a convective unstable condition (pseudo-equivalent potential temperature decreased with height), and 42 min before the initiation of the isolated convection, there was a high pseudo-equivalent potential temperature center greater than 360 K in the lower layer of the TUR, increasing the vertical gradient of the pseudo-equivalent potential temperature over the TUR, which was conducive to the initiation and development of the convection.

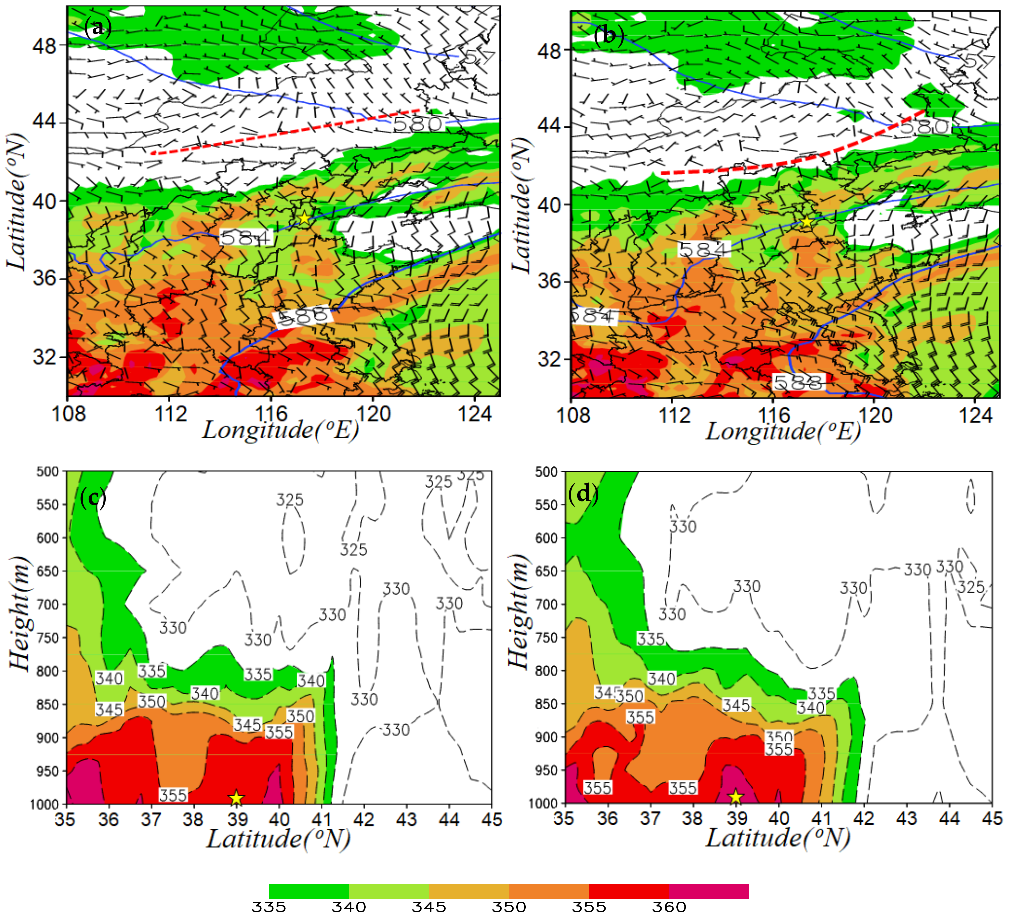

Figure 4. Pseudo-equivalent potential temperature (colored, unit: K) at 850 hPa, horizontal wind barbs at 925 hPa, and geopotential height (solid contour, unit: dgpm) at 500 hPa at (**a**) 14:00 BT and (**b**) 17:00 BT on 1 August 2019; the red dashed lines represent convergence line at 925 hPa. Cross-section of the pseudo-equivalent potential temperature (colored and dash contour, unit: K) along 117° E at (**c**) 14:00 BT and (**d**) 17:00 BT on 1 August 2019. The yellow pentagram is used to indicate the position of the TUR.

There is no sounding station in Tianjin City. When analyzing and researching the strong convection case, Beijing or Laoting sounding closing to Tianjin are usually used. However, in fact, these two soundings are more than 100 km away from Tianjin, which is difficult to really reflect the atmospheric structure over Tianjin. Therefore, the hourly temperature, wind, humidity and pressure of surface meteorology observation stations in the TUR were combined with the ERA5 data of the adjacent grid points (117° E, 39° N) above the boundary layer to form the hourly sounding data (see Figure 5), which was analyzed to further investigate the dynamic and thermodynamic conditions for the initiation and development of the isolated convection in the TUR. Three hours before the initiation of the isolated convection (see Figure 5a), the temperature lapse rate in the lower troposphere over the TUR was higher than the dry adiabatic lapse rate, which means that the atmosphere in the TUR was absolutely unstable. At the same time, the convective inhibition (CIN) was 0 J/kg, the lifting condensation level (LCL) was only 827.5 hPa, and the convective available potential energy (CAPE) reached 2375 J/kg, which suggests that the atmospheric conditions around the TUR were greatly beneficial to convective triggering with very little lifting force required. The precipitable water was 43.76 mm, which means that the water vapor condition over the TUR was not bad. During the initiation period of the isolated convection (see Figure 5b), the atmosphere in the TUR was still absolutely unstable (CIN = 0 J/kg). In addition, the CAPE was further increased to 3771 J/kg, and the precipitable water increased to 47.11 mm, indicating that the atmospheric conditions were quite favorable to convective triggering and maintenance. Significantly, it can be seen from Figure 5 that the vertical shear of wind was relatively weak at a lower troposphere, barely reaching 4 m·s^{-1} between 1000 hPa to 850 hPa before the initiation of the isolated convection.

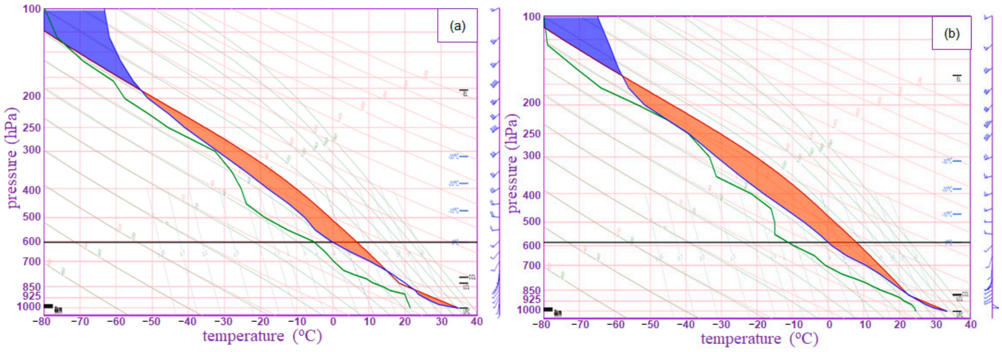

Figure 5. Vertical profiles of temperature (blue line, unit: °C), dew point temperature (green line, unit: °C), and the temperature of adiabatic rise curve of surface air envelope (brown line, unit: °C) above the TUR on the T-logp map (surface observations combined with ERA5 reanalysis data above the boundary layer) at (**a**) 14:00 BT and (**b**) 17:00 BT on 1 August 2019, respectively.

In summary, although the wind speed of airflow and the vertical shear of horizontal wind were relatively weak, the atmospheric thermodynamic conditions promoted the start-up of the isolated convection in the TUR. However, because of the absence of a significant synoptic scale lifting mechanism in the TUR, and the initiation of the isolated convection cannot be related to the dynamic system, we hypothesize that some small or mesoscale weather system might be responsible for the precise location and timing of the isolated convection occurrences. Based on the analysis of the surface meteorological elements seen by surface observations and the reflectivity detected by the Doppler Radar, we demonstrate in the following section that the sea breeze front and gust front were key to the occurrence and development of the isolated convection around the TUR in the context of the UHHI effect.

5. Initiation of the Isolated Convection

Figure 6a shows the composite reflectivity at 17:42 BT and surface wind at 17:00 BT on 1 August 2019, and Figure 6b shows an enlarged view of the red dashed box in Figure 6a. As shown in Figure 6a, at 17:00 BT, the gust front (blue dashed line) was formed and its formation was related to the previous convections, which was 20–30 km away from the TUR. Meanwhile, there was velocity convergence in easterly (sea-breeze) front around the TUR at 17:00 BT, where the isolated convection was observed at 17:42 (see Figure 6b). That is to say, the sea-breeze front was the key mesoscale system, which was conductive to the isolated convection's initiation there. Figure 6c shows the composite reflectivity and surface wind at 18:00 BT on 1 August 2019, and Figure 6d shows an enlarged view of the blue dashed box in Figure 6c. As is shown in Figure 6c,d, at 18:00 BT, the gust front moved northward, and the sea breeze front moved westward. As a result, the gust front influenced the isolated convection and collided with the sea breeze front around the TUR, making five reflectivity centers of convection merge and strengthen rapidly. At 18:00 BT, there were five echo centers greater than 40 dBz, and by 18:30, they had merged into an isolated convection with an echo center greater than 55 dBz (see Figure 3g).

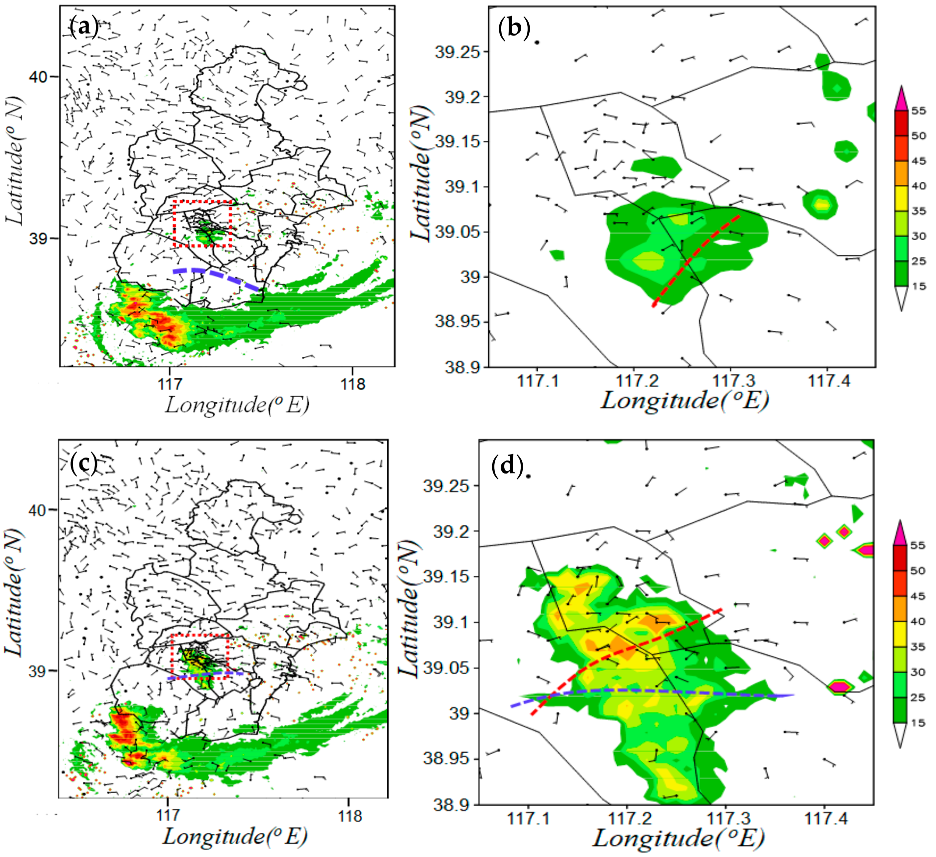

Figure 6. (**a**) Composite reflectivity (colored, unit: dBZ) at 17:42 BT and surface wind (barb, unit: m·s^{-1}) at 17:00 BT on 1 August 2019. (**b**) Enlarged view of the red dashed box in (**a**). (**c**) Composite reflectivity (colored, unit: dBZ) and surface wind (vector, unit: m·s^{-1}) at 18:00 BT on 1 August 2019; (**d**) Enlarged view of the red dashed box in (**c**); the blue dashed line is the gust front and the red dashed line is the sea breeze front.

Figure 7a–f are the distributions of surface temperature, dew-point temperature and pseudo-equivalent potential temperature. As shown in Figure 7a–c, at 17:00 BT, due to the evaporative cooling caused by previous convections and clouds shielding from solar heating, the temperature fields at the surface exhibited a quasi-circular area of lower temperature (the center below 26 °C) to the South of Tianjin and there were also low value centers of dew point temperature (see Figure 7b) and pseudo-equivalent temperature (see Figure 7c) in close proximity to the same location. At the same time, there was a high temperature area extending from West to East at nearly 39° N, with a high value center of more than 34 degrees, which is located to the west of the TUR, and the TUR is located at the east edge of the high temperature area (see Figure 7a). As shown in Figure 7b, there was a large dew point temperature area extending from southeast to northwest, and the TUR was also located at northwest edge of the high dew point temperature area. As a result, the TUR was located at the intersection of the high temperature area and high dew point temperature area. That is to say, the thermal characteristics of the TUR were high temperature and high humidity. As shown in Figure 7c, the pseudo-equivalent potential temperature center was located around the TUR, with a central value of 383 K, which can be defined as the UHHI effect, while the low value center of the pseudo-equivalent potential temperature was formed by early precipitation to the south of Tianjin, with a central value lower than 350 K, forming a strong thermal gradient and providing better thermodynamic conditions for the initiation of the isolated convection. As shown in Figure 7d–f, the thermal conditions at 18:00 BT were basically the same as those at 17:00 BT, while the cold pool to the south of Tianjin was more powerful. Corresponding to the further northward advance of the gust front, the high center of pseudo-equivalent potential temperature moved slightly northward, but it was still around the TUR, providing the thermal conditions for the further development and strengthening of the isolated convection. This suggests that, in addition to the gust front at the boundary layer, the baroclinic zone also moved northward during the development of the isolated convection. As shown in Figure 4c,d, the pseudo-equivalent potential temperature decreased with height, which means the atmosphere of the middle level and low level were always in a convective unstable condition. That is to say, the UHHI effect, corresponding to the high center of pseudo-equivalent potential temperature at the surface, strengthened the local instability around the TUR. So, the atmospheric thermodynamic conditions around the TUR were more conducive to the initiation of convection than those in rural areas.

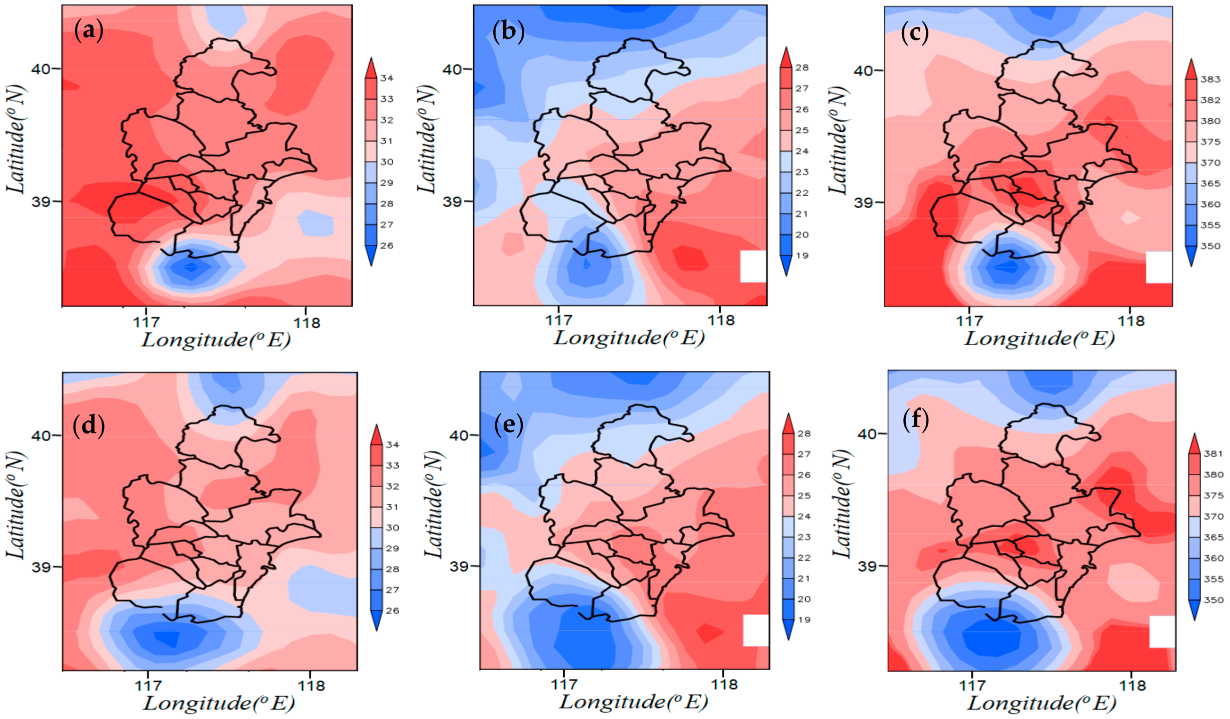

Figure 7. Distribution of surface temperature (colored, unit: °C): (**a**) 17:00 BT and (**d**) 18:00 BT. Distribution of surface dew point temperature (colored, unit: °C): (**b**) 17:00 BT and (**e**) 18:00 BT. Distribution of surface pseudo-equivalent potential temperature (colored, unit: K): (**c**) 17:00 BT and (**f**) 18:00 BT.

Thus, it can be seen that the isolated convection around the TUR that happened in the evening of 1 August 2019 was initiated and developed due to the interaction of the sea breeze front and gust front in the context of the UHHI effect. The sea breeze front approached the TUR and triggered the convection around the TUR in the context of the UHHI effect. The gust front produced by the early heavy precipitation played a vital role in the merging of the convection's five echo centers and the development of the isolated convection.

6. Splitting of Isolated Convection

Figure 8 is the composite reflectivity and surface wind at 19:00 BT on 1 August 2019. As shown in Figure 8, at 19:00 BT, the reflectivity center of the isolated convection (convection A) was located in the west of the TUR, and the value of reflectivity reached more than 55 dBz. Corresponding to the center of reflectivity, there was a divergent center of the surface wind field, and its eastward divergent air flow had shear with the environmental air flow (see Figure 8b), leading to a new convection (convection B) being triggered in the east of the TUR at 19:06 BT (see Figure 9a), and the reflectivity center reaching more than 50 dBz. As shown in Figure 9b–d, between 19:12 BT and 19:24 BT, the intensity and area of convection B increased continuously, while convection A moved to the northeast, whose intensity and area decreased gradually.

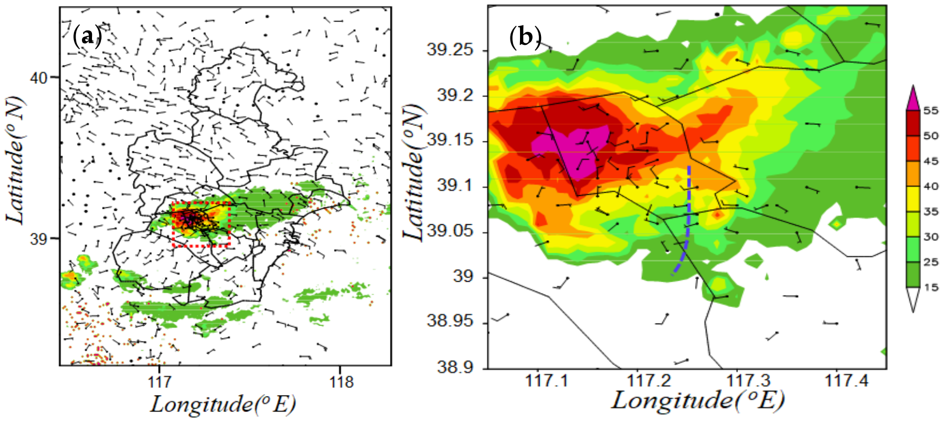

Figure 8. (**a**) Composite reflectivity (colored, unit: dBZ) and surface wind (vector, unit: m·s^{-1}) at 19:00 BT on 1 August 2019. (**b**) Enlarged view of the red dashed box in Figure 9a, and the blue dashed line is the gust front.

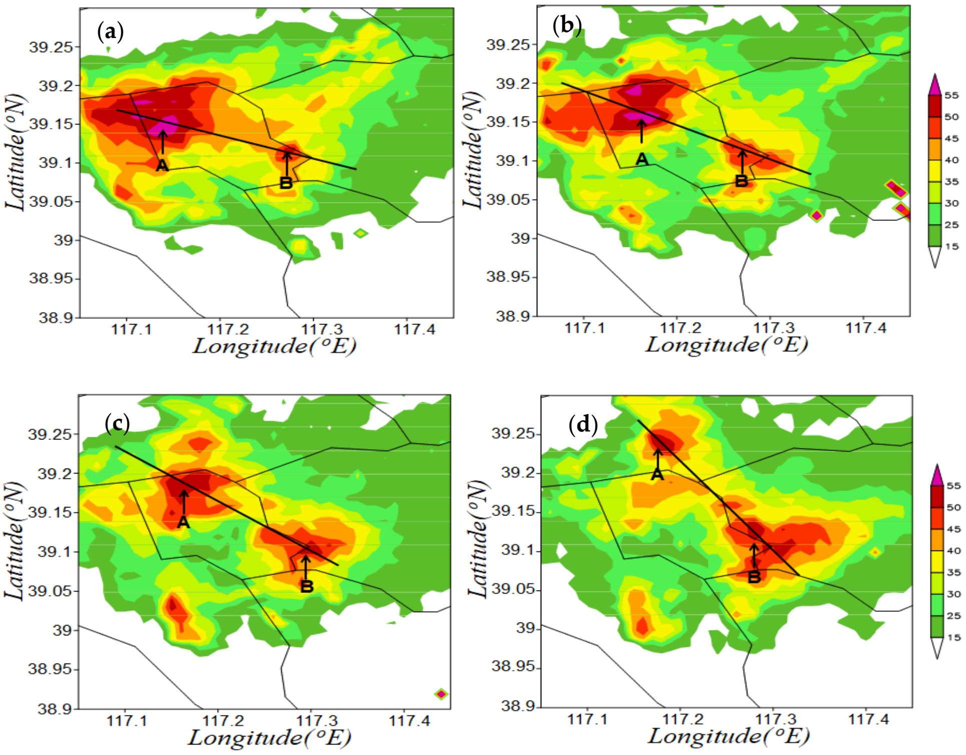

Figure 9. Composite reflectivity (colored, unit: dBZ) at (**a**) 19:06 BT, (**b**) 19:12, (**c**) 19:18 and (**d**) 19:24 on 1 August 2019. The cross section of reflectivity in Figure 10 moves along these thick solid black lines, and "A" and "B" represent the position of two convections.

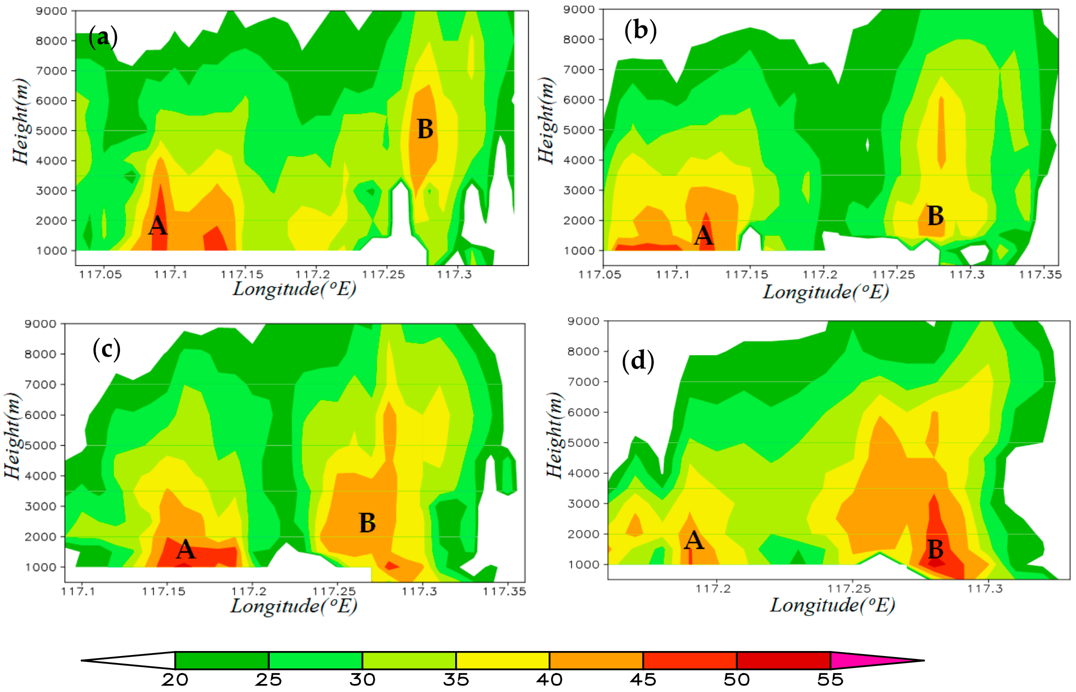

Figure 10. Cross section of reflectivity (colored, unit: dBZ) along the solid lines in Figure 10: (**a**) 19:06, (**b**) 19:12, (**c**) 19:18 and (**d**) 19:24 BT on 1 August 2019. "A" and "B" represent the position of two convections.

Figure 10a–d are the cross sections of the reflectivity along the solid lines in Figure 9a–d. As shown in Figure 10, at 19:06 BT (see Figure 10a), convection B was formed. The echo center was at the height of 3–6 km. At 19:12 BT (see Figure 10b), convection B continued to strengthen and the echo center was at the height of 1 km (the lowest height at which the echo can be detected by the Tanggu Radar at this position). After that (see Figure 10c,d), convection B continued to strengthen, the echo center was still at the height of 1 km, and reflectivity of the echo center increased to more than 50 dBz. However, convection A continued to weaken.

7. Discussion

In the current research, the triggering and development of the isolated convection around the TUR had a close relationship with the interaction of the sea breeze front and gust front in the context of the UHHI effect. Previous research results show that the convections were more likely to form at the crossing point of the collision between the gust front and sea breeze front, and the convections occurred after the collision of the sea breeze front and gust front [6,39]. The literature [6] further revealed the physical characteristics of convections at the collision intersection through numerical simulation, that is, there are obvious vertical motion and convergence characteristics, and the distribution characteristics of the generalized Richardson number are also significant, whose thickness is about 1.0 KM, and the CAPE value increased significantly before the initiation of convections. However, another phenomenon was identified in our research, and we present some interesting findings. The isolated convection was first triggered by the sea breeze front, and then the gust front advanced to the convection area and interacted with the sea breeze front, resulting in the merging of multiple convective cores in the isolated convection and the continuous strengthening of the isolated convection.

The UHI effect refers to the temperature in the urban region being significantly higher than that in the rural region. The investigation of a UHI event showed that the interactions between the UHI effect and the sea breeze front indeed existed [44,55]. Previous research shows that the high-temperature area of the UHI effect could provide favorable thermodynamic conditions for the isolated convections [13]. However, another phenomenon was identified in our research, which is also worthy of our attention, that is, that the urban region is not located in the center of high temperature, but is located around the center of high pseudo-equivalent potential temperature, indicating that the urban region has the characteristics of high temperature and high humidity compared with the surrounding rural area. As described in Section 4 of this paper, this meteorological condition is also conducive to forming unstable conditions and providing favorable thermal conditions for the initiation and development of strong convective weather, which played the same role as the UHI effect. However, this phenomenon does not meet the definition of the UHI effect. In order to better explain the physical mechanism of the isolated convection in urban regions, this phenomenon was defined as the phenomenon of urban humid heat island (UHHI) in this paper.

As is well known, it is very challenging for the most advanced numerical weather prediction (NWP) models to forecast the accurate position and time of isolated convection around urban regions. Real-time surface observations, radar measurements and other observations can help to reveal the mechanism of isolated convection. In our forthcoming study, more cases of isolated convection will be collected and analyzed to further examine the roles of the UHI (or UHHI) effect, mesoscale boundary and convective interaction in determining the CI timing and location of the isolated convection around the TUR.

8. Conclusions

The isolated convection was observed in the TUR on 1 August 2019. The present study analyzed the ERA5 reanalysis data, the surface meteorological elements data observed by surface observations, and the reflectivity detected by the Tanggu S-band Radar, and discussed the mechanisms that led to the initiation, maintenance, and development of the isolated convection. The main conclusions are summarized as follows:

(1) This isolated convection event occurred about 250 km away from a low-level convergence line to the north and in the warm and humid area dominated by southerly flow at a low level. The vertical shear of wind velocity at a low level was not obvious (mostly less than 4 $m \cdot s^{-1}$ between 1000 hPa and 850 hPa), but the atmospheric thermodynamic conditions (i.e., the CAPE of more than 3500 J/kg and CIN of nearly zero) were beneficial for the triggering and development of the isolated convection.

(2) Moreover, 42 min before the initiation of the isolated convection, the sea-breeze front started to influence the TUR and continued to move west. At the same time, the TUR was located at the intersection of the high temperature band and high dew point temperature band, with characteristics of high temperature and high humidity. The surface pseudo-equivalent potential temperature around the TUR was more than 383 K, with 2–3 K contrast of the surrounding area, forming the UHHI effect. That is to say, the sea breeze front triggered the isolated convection around the TUR in the context of the UHHI effect.

(3) The gust front was formed between the cold pool and the warm and humid air of UHHI at 17:00 BT on 1 August 2019. The formation of cold pool was caused by the previous convections, which was 20–30 km away from the TUR. After the initiation of the isolated convection (18:00 BT), the gust front moved northward, started to influence the convection and collided with the sea breeze front, which made the many convections merge into an isolated convection. In the following 30 min (from 18:00 to 18:30 BT), the convection developed continuously and grew into its mature stage with the interaction of the sea breeze front and gust front. Maybe the gust front was not the direct reason of the isolated convection's initiation, but rather the gust front moving northward, approaching the convection and interacting with the sea breeze front, resulted in convections merging into an isolated convection and the convection's development.

(4) Due to the heavy precipitation produced by the isolated convection, a new cold pool was formed around the TUR. The westerly cold outflow subsequently met with easterly winds, leading to a new convection being triggered in the east of the TUR. Subsequently, the old convection continued to weaken, and the new convection continued to strengthen, but it also weakened and disappeared at 20:36 BT.

Author Contributions: Methodology: Y.W. and N.Z.; analysis of the results: Y.W. and N.Z.; writing and figures: N.Z.; data processing: N.Z. and X.L. All authors have read and agreed to the published version of the manuscript.

Funding: This work was supported by the National Key Research and Development Program of China (2019YFC1510105), National Natural Science Foundation of China (41675046), the Natural Science Foundation of Tianjin (Youth Program) in China (18JCQNJC09300), Forecaster Program of China Meteorological Administration (CMAYBY2020-009, CMAYBY2016-006), and the Project of Tianjin Meteorological Administration (202106ybxm01).

Institutional Review Board Statement: Not applicable.

Informed Consent Statement: Not applicable.

Data Availability Statement: Not applicable.

Conflicts of Interest: The authors declare no conflict of interest.

References

1. Duan, L.; Bian, S.F.; Yu, X.D.; Cui, Y.Y. Comparative Analysis of CINRAD SA Doppler Radar Product in Three Local Torrential Rains in the West of Beijing. *Meteorol. Mon.* **2009**, *35*, 21–28. [CrossRef]
2. Guo, H.; Duan, L.; Yang, B.; Bian, S.F.; Li, J. Mesoscale and Microscale Analysis on a Local Torrential Rain Event in Fragrant Hills Area of Beijing on July 9, 2006. *J. Appl. Meteorol. Sci.* **2008**, *19*, 265–275.
3. Zhang, N.; He, Q.Y.; Liu, B.X.; Wu, Z.L.; Liu, Y.W. Analysis on the mesoscale characteristics of a local rainstorm event under a typical circulation situation in Tianjin. *Torrential Rain Disasters* **2018**, *37*, 230–237. [CrossRef]
4. Wei, Y.H.; Chen, H.; He, Q.Y.; Lin, X.M.; Zhang, H. Influence of Easterly Winds from West Coast of Bohai Sea on Local Heavy Rainfall in Tianjin. *Meteorol. Mon.* **2019**, *45*, 61–72. [CrossRef]
5. Zhang, N.; Yang, X.J.; Qiu, X.B.; Liu, Y.W.; Yang, Y. Mechanism Analysis and Rethinking of Short-Term Prediction of a Sudden Rainstorm. *Meteorol. Mon.* **2018**, *44*, 118–131. [CrossRef]
6. Wang, Y.; Gao, S.T.; Liang, Z.M. Analysis on the Observation and Simulation of Thunderstorms Triggered by Sea Breeze Front in Bohai Bay. *Plateau Meteorol.* **2014**, *33*, 848–854. [CrossRef]
7. Du, Y.; Chen, G. Heavy rainfall associated with double low-level jets over Southern China. Part II: Convection initiation. *Mon. Weather Rev.* **2019**, *147*, 543–565. [CrossRef]
8. Kain, J.S.; Coniglio, M.C.; Correia, J.; Clark, A.J.; Marsh, P.T.; Ziegler, C.L.; Lakshmanan, V.; Miller, S.D.; Dembek, S.R.; Weiss, S.J.; et al. A feasibility study for probabilistic convection initiation forecasts based on explicit numerical guidance. *Bull. Am. Meteorol. Soc.* **2013**, *94*, 1213–1225. [CrossRef]
9. Lock, N.A.; Houston, A.L. Empirical examination of the factors regulating thunderstorm initiation. *Mon. Weather Rev.* **2014**, *142*, 240–258. [CrossRef]
10. Ukkonen, P.; Manzato, A.; Makela, A. Evaluation of thunderstorm predictors for Finland using reanalyses and neural networks. *J. Appl. Meteorol. Climatol.* **2017**, *56*, 2335–2352. [CrossRef]
11. Zhang, Y.; Zhang, F.; Stensrud, D.J.; Meng, Z. Intrinsic predictability of the 20 May 2013 tornadic thunderstorm event in Oklahoma at storm scales. *Mon. Weather Rev.* **2016**, *144*, 1273–1298. [CrossRef]
12. Li, H.Q.; Cui, X.P.; Zhang, D.L. On the initiation of an isolated heavy-rain producing storm near the central urban area of Beijing metropolitan region. *Mon. Weather Rev.* **2017**, *145*, 181–197. [CrossRef]
13. Zhang, N.; Wang, Y. Mechanisms for the isolated convections triggered by the sea breeze front and the urban heat Island. *Meteorol. Atmos. Phys.* **2021**, *133*, 1143–1157. [CrossRef]
14. Shepherd, J.M.; Burian, S.J. Detection of urban induced rainfall anomalies in a major coastal city. *Earth Interact.* **2003**, *7*, 1–17. [CrossRef]
15. Shepherd, J.M. A review of current investigations of urbaninduced rainfall and recommendations for the future. *Earth Interact.* **2005**, *9*, 1–27. [CrossRef]
16. Kaufmann, R.K.; Seto, K.C.; Schneider, A.; Liu, Z.; Zhou, L.; Wang, W. Climate response to rapid urban growth: Evidence of a human-induced precipitation deficit. *J. Clim.* **2007**, *20*, 2299–2306. [CrossRef]
17. Kishtawal, C.M.; Niyogi, D.; Tewari, M.; Pielke, R.A.; Shepherd, J.M. Urbanization signature in the observed heavy rainfall climatology over India. *Int. J. Climatol.* **2010**, *30*, 1908–1916. [CrossRef]
18. Yu, R.; Jiang, Z.; Zhai, P. Impact of urban land-use change in eastern China on the East Asian subtropical monsoon: A numerical study. *J. Meteor. Res.* **2016**, *30*, 203–216. [CrossRef]
19. Zhang, D.L. Rapid urbanization and more extreme rainfall events. *Sci. Bull.* **2020**, *65*, 516–518. [CrossRef]
20. Zhang, D.L.; Jin, M.S.; Shou, Y.; Dong, C. The influences of urban building complexes on the ambient flows over the Washington–Reston region. *J. Appl. Meteor. Climatol.* **2019**, *58*, 1325–1336. [CrossRef]
21. Jiang, X.; Luo, Y.; Zhang, D.L.; Wu, M. Urbanization enhanced summertime extreme hourly precipitation over the yangtze river delta. *J. Clim.* **2020**, *33*, 5809–5826. [CrossRef]

22. Byers, H.R.; Rodebush, H.R. Causes of thunderstorms of the Florida Peninsula. *J. Meteor.* **1949**, *5*, 275–280. [CrossRef]
23. Dong, G.H.; Liu, Y.W.; Sun, M.N.; Dai, Y.W. Effect of Urban Heat Island and Sea Breeze Front Superimposition on a Local Heavy Rainfall. *Meteorol. Mon.* **2013**, *39*, 1422–1430. [CrossRef]
24. Hane, C.E.; Ziegler, C.L.; Bluestein, H.B. Investigation of the dry line and convective storms initiated along the dry line: Field experiments during COPS-91. *Bull. Amer Meteor. Soc.* **1993**, *74*, 2133–2145. [CrossRef]
25. Koch, S.E.; Ray, C.A. Mesoanalysis of summertime convergence zones in central and eastern North Carolina. *Weather Forecast.* **1997**, *12*, 56–77. [CrossRef]
26. Purdom, J.F.W. Some uses of high resolution GOE Simagery in the mesoscale forecasting of convection and its behavior. *Mon. Weather Rev.* **1976**, *104*, 1474–1483. [CrossRef]
27. Rhea, J.O. A study of thunderstorm formation along dry lines. *J. Appl. Meteorol.* **1966**, *5*, 58–63. [CrossRef]
28. Wang, J.H.; Zhang, N.; Miao, C.S.; Shou, S.W. The analysis of a strong convective precipitation process in Tianjin on 25 June 2008. *Trans. Atmos. Sci.* **2011**, *34*, 688–696. [CrossRef]
29. Wilson, J.W.; Megenhardt, D.L. Thunderstorm initiation, organization, and lifetime associated with Florida boundary layer convergence lines. *Mon. Weather Rev.* **1997**, *125*, 1507–1525. [CrossRef]
30. Wilson, J.W.; Schreiber, W.E. Initiation of convective storms at radar-observed boundary-layer convergence lines. *Mon. Weather Rev.* **1986**, *114*, 2516–2536. [CrossRef]
31. Ziegler, C.L.; Rasmussen, E.N. The initiation of moist convection at the dry line: Forecasting issues from a case perspective. *Weather Forecast.* **1998**, *13*, 1106–1131. [CrossRef]
32. Miao, J.F. An overview of numerical studies of interaction of urban heat island and sea breeze circulations. *Trans. Atmos. Sci.* **2014**, *37*, 521–528. [CrossRef]
33. Su, T.; Miao, J.F.; Han, F.R. An Overview of Observational and Numerical Studies of Sea Breeze Thunderstorms. *Meteorol. Sci. Technol.* **2016**, *44*, 47–54.
34. He, Q.Y.; Xie, Y.Y.; Dong, G.H.; Liu, Y.W.; Sun, Y.X. The Role of Sea Land Breeze Circulation in Local Convective Torrential Rain Happening in Tianjin on 26 September 2009. *Meteorol. Mon.* **2011**, *37*, 291–297. [CrossRef]
35. Liang, Z.M.; Gao, S.T.; Wang, Y. Data Analysis of Collision-Type Sea-Breeze Front in the Bohai Bay Region. *Clim. Environ. Res.* **2013**, *18*, 607–616. [CrossRef]
36. Lu, H.Z.; Liu, Y.W.; Liu, A.X.; Zhang, N.; Sun, M.N. Study of Thunderstorm Initiation and Intensification Rules Associated with Sea Breeze Fronts. *Meteorol. Mon.* **2012**, *38*, 1078–1086. [CrossRef]
37. Fovell, R.G. Convective Initiation ahead of the Sea-Breeze Front. *Mon. Weather Rev.* **2005**, *133*, 291–300. [CrossRef]
38. Dailey, P.S.; Fovell, R.G. Numerical simulation of the interaction between the sea-breeze front and horizontal convective rolls. *Mon. Weather Rev.* **1999**, *127*, 858–878. [CrossRef]
39. Fu, S.; Rotunno, R.; Xue, H.W.; Chen, J.H.; Deng, X. A large-eddy simulation study of deep-convection initiation through the collision of two sea-breeze fronts. *Atmos. Chem. Phys.* **2021**, *21*, 9289–9308. [CrossRef]
40. Simpson, M.; Raman, S.; Suresh, R.; Mohanty, U.C. Urban effects of Chennai on sea breeze induced convection and precipitation. *J. Earth Syst. Sci.* **2008**, *117*, 897–909. [CrossRef]
41. Dong, G.H.; He, Q.Y.; Liu, Y.W.; Xie, Y.Y.; Dai, Y.W. The Role of Sea Breeze Front in Local Storm of Bohai Coast. *Meteorol. Mon.* **2011**, *37*, 1100–1107. [CrossRef]
42. Yi, X.Y.; Liu, Y.W.; Sun, M.N.; Dong, G.H.; Li, Q.C. Analysis on Dynamical and Thermodynamic Process of Thunderstorms Triggered and Merged by Sea Breeze Convergence Lines. *Meteorol. Mon.* **2014**, *40*, 1539–1548. [CrossRef]
43. Gedzelman, S.D.; Austin, S.; Cermak, R.; Stefano, N.; Partridge, S.; Quesenberry, S.; Robinson, D.A. Mesoscale aspects of the Urban Heat Island around New York City. *Theor. Appl. Climatol.* **2003**, *75*, 29–42. [CrossRef]
44. Shen, L.X.; Zhao, C.F.; Ma, Z.S.; Li, Z.Q.; Li, J.P.; Wang, K.C. Observed decrease of summer sea-land breeze in Shanghai from 1994 to 2014 and its association with urbanization. *Atmos. Res.* **2019**, *227*, 198–209. [CrossRef]
45. Wang, Y.; Zhao, K.; Xie, T. *Research and Application of Early Warning Technology for Thunderstorm Triggered by Sea Breeze Front*; China Meteorological Press: Beijing, China, 2020; pp. 31–32. ISBN 978-7-5029-7348-3.
46. Yoshikado, H. Numerical study of the daytime urban effect and its interaction with the sea breeze. *J. Appl. Meteorol.* **1992**, *31*, 1146–1164. [CrossRef]
47. Yoshikado, H. Interaction of the sea breeze with urban heat islands of different sizes and locations. *J. Meteorol. Soc. Jpn.* **1994**, *72*, 139–142. [CrossRef]
48. Hersbach, H.; Bell, B.; Berrisford, P.; Hirahara, S.; Thépaut, J. The ERA5 global reanalysis. *Q. J. R. Meteorol. Soc.* **2020**, *146*, 1999–2049. [CrossRef]
49. Brooks, H.E.; Lee, J.W.; Craven, J.P. The spatial distribution of severe thunderstorm and tornado environments from global reanalysis data. *Atmos. Res.* **2003**, *67*, 73–94. [CrossRef]
50. Brooks, H.E.; Anderson, A.R.; Riemann, K.; Ebbers, I.; Flachs, H. Climatological aspects of convective parameters from the NCAR/NCEP reanalysis. *Atmos. Res.* **2007**, *83*, 294–305. [CrossRef]
51. Markowski, P.M.; Hannon, C.; Frame, J.; Lancaster, E.; Pietrycha, A.; Edwards, R.; Thompson, R.L. Characteristics of vertical wind profiles near supercells obtained from the Rapid Update Cycle. *Weather Forecast.* **2003**, *18*, 1262–1272. [CrossRef]
52. Thompson, R.L.; Edwards, R.; Hart, J.A.; Elmore, K.L.; Markowski, P. Close proximity soundings within supercell environments obtained from the Rapid Update Cycle. *Weather Forecast.* **2003**, *18*, 1243–1261. [CrossRef]

53. Thompson, R.L.; Mead, C.M.; Edwards, R. Effective storm-relative helicity and bulk shear in supercell thunderstorm environments. *Weather Forecast.* **2007**, *22*, 102–115. [CrossRef]
54. Allen, J.T.; Karoly, D.J. A climatology of Australian severe thunderstorm environments 1979–2011: Inter-annual variability and ENSO influence. *Int. J. Climatol.* **2014**, *34*, 81–97. [CrossRef]
55. Bauer, T.J. Interaction of Urban Heat Island Effects and Land-Sea Breezes during a New York City Heat Event. *J. Appl. Met. Clim.* **2020**, *59*, 477–495. [CrossRef]